Research Article | Vol. 12, No. 11 / 1 Nov 2021 / Biomedical Optics Express 7244
Biomedical Optics EXPRESS

Performance improvement of a silicon nitride ring resonator biosensor operated in the TM mode at 1310 nm

LUCÍA CASTELLÓ-PEDRERO, MARÍA I. GÓMEZ-GÓMEZ, JAIME GARCÍA-RUPÉREZ, AMADEU GRIOL, AND ALEJANDRO MARTÍNEZ*

Nanophotonics Technology Center, Universitat Politècnica de València, Camino de Vera s/n, Building 8F, 46022 Valencia, Spain
amartinez@ntc.upv.es

Abstract: Silicon-based ring resonators have been demonstrated to be a key element to build lab-on-chip devices due to their ability to perform as label-free photonic sensors. In this work, we demonstrate photonic biosensing using silicon nitride ring resonators operated in the TM mode around 1310 nm wavelengths. Our results show that operating the devices using the TM mode results in an increased sensitivity in comparison with the typically used TE mode, while working at 1310 nm wavelengths compared to 1550 nm contributes to an increased quality factor. As a result, a reduction in the intrinsic limit of detection is achieved, indicating the suitability of TM modes in the 1310 nm regime for biosensing using integrated photonics.

1. Introduction

Silicon photonics is becoming the mainstream technology in integrated optics because it enables massive fabrication of devices at low cost by using standard CMOS fabrication tools. Amongst the myriad of foreseen applications, the implementation of highly-sensitive label-free sensing on silicon chips is enabling the long-pursued paradigm of lab-on-chip [1]. Indeed, silicon-based lab-on-chip devices could be massively used for applications such as early diagnosis or gas detection with the advantages of being ultra-compact, lightweight, handled by non-specialists and ultimately disposable [2,3].

A silicon-based photonic sensor includes a photonic structure whose optical response changes when the refractive index of its surroundings is modified. Therefore, it is essentially a refractometric sensor that operates in a label-free way [3]. There are several photonic structures that can be used to this end, including photonic crystal cavities [4] and waveguides [5], Mach-Zehnder interferometers [6], disks [7] and ring resonators [8]. Waveguide ring resonators (RRs) constitute a compact circular sensing element which provides a fast readout and presents a high degree of integration with other optical and fluidic components. Moreover, the fact that waveguide RRs can be fabricated with standard semiconductor processing technologies favours mass production at low cost [4]. The silicon microfabrication methods used to manufacture RR sensors can replicate identical units, enabling the production of RR sensor arrays, which achieve a higher level of parallelisation.

The traditional silicon on insulator (SOI) substrates exhibit a high index contrast between silicon and silicon dioxide (relative refractive index difference of 0.41), enabling a tight light confinement in the waveguide core. Nevertheless, this also implies a higher sensitivity to common fabrication imperfections like surface roughness [9], which results in non-negligible propagation losses. On the other hand, silicon nitride (Si_3N_4) has still a higher refractive index than silicon dioxide but not as high as silicon, implying a lower index contrast (relative refractive index difference of 0.24). Therefore, using Si_3N_4 as core material renders the waveguiding mechanism

#437823 https://doi.org/10.1364/BOE.437823
Journal © 2021 Received 16 Jul 2021; revised 15 Sep 2021; accepted 15 Sep 2021; published 1 Nov 2021

Biomedical Optics EXPRESS

less prone to scattering losses associated with sidewall roughness and increases the tolerance to dimensional deviations during fabrication. Hence, Si_3N_4 waveguides exhibit propagation losses almost an order of magnitude lower than their silicon counterparts [10], as well as remaining low cost and allowing a reasonable level of integration [11,12]. In addition, Si_3N_4 presents potential advantages for sensing applications [13,14], since it is resistant to diffusion of moisture and sodium ions, thus maintaining a stable refractive index even when exposed to biochemical fluids.

Improving the performance of optical biosensors in terms of sensitivity, quality factor and limit of detection is required for label-free sensing in complex samples, notably in medical diagnostic applications [15]. Optical component optimisation and design, including polarisation, wavelength, and waveguide geometry and configuration can contribute to enhancing the overall performance of the biosensor. Additionally, in the context of lab-on-chip applications, the commercialisation of the biosensing device implies satisfying the market demands, hence reaching a trade-off between performance and production cost.

An increased sensitivity can be achieved, amongst other means, by employing different waveguide modes that interact in different ways with the waveguide surroundings. In integrated photonics, the two fundamental guided modes are usually termed transverse electric (TE) and transverse magnetic (TM). Whilst for TE modes the main component of the electric field is parallel to the substrate, for TM modes this component is perpendicular to the chip plane. Therefore, the main difference in the electric field intensity distributions of the TE and TM modes propagating in a rectangular-core waveguide - whose width is larger than its thickness - is that most of the field intensity is located above and beneath the waveguide core (in the cladding and substrate) for the TM mode, presenting a stronger light-matter interaction. Therefore, photonic sensors operating at TM mode have a larger evanescent field component above the waveguide, offering an improved sensitivity compared to the TE mode counterparts. Moreover, the TM mode also encounters less scattering loss, which is mainly caused by sidewall roughness, compared to the TE mode [16]. Notice that TE and TM modes can be defined differently in other photonic systems, such as dielectric spheres, which can also be used for sensing purposes [17].

Furthermore, the quality factor of a RR, which represents the total distributed loss of the cavity, can be modified in various ways. There are several sources of loss, including material absorption and scattering (both within the silicon-based waveguide and in the aqueous analyte cladding), waveguide radiation and scattering, mode mismatch and substrate leakage [2]. Therefore, reducing bending and scattering losses [7] or absorption loss in the bulk solution [2] can improve the quality factor of a sensor. Water absorption from aqueous analytes is a major source of loss for silicon photonic biosensors operating at 1550 nm wavelengths. It has been reported that losses due to water absorption are approximately 10 times lower around 1310 nm compared to 1550 nm wavelengths [18,19], which should result in higher Q factors. The practical convenience of using a wavelength of 1310 nm should be noted, since it also lies within the telecommunications band and laser access and price are comparable to the ones typically used in the 1550 nm range.

However, despite the advantages, demonstration of refractometric sensing at 1310 nm using silicon nitride RRs operating in the TM mode has not yet been proved. Here, we demonstrate the performance improvement of a RR sensor in terms of sensitivity, quality factor and limit of detection by using TM-polarised light at 1310 nm wavelengths, compared to the same device when operated with the TE mode at 1550 nm wavelengths.

2. Ring resonators as sensing elements

In RRs, light propagates in the form of circulating waveguide modes, which are usually either TE or TM. Such guided modes are supported along the circumference of the cavity according to the resonance condition, satisfied when the optical length of the resonator is equal to an integer

Biomedical Optics EXPRESS

multiple of the wavelengths [16]:

$$\lambda_{\text{res}} = \frac{Ln_{\text{eff}}}{N} \tag{1}$$

where λ_{res} is the sensor's resonance wavelength, N is an integer, L is the RR round trip and n_{eff} is the effective refractive index of the guided mode. The circulating waves interfere constructively at the resonance wavelengths. The local accumulation due to selective binding of target molecules to a biorecognition layer deposited over the waveguide RR produces a modification in the effective refractive index of the guided mode. This red-shifts the resonance, which is measured in the transmission of the bus waveguide and leveraged for biosensing. The integer-dependence of the resonance condition given in Eq. (1) implies that multiple resonances are supported, and the distance in free space wavelength between resonances, or free spectral range (FSR), depends on the RR optical length as [20]:

$$\text{FSR} = \frac{\lambda^2}{n_g L} \tag{2}$$

where λ is the free space wavelength and n_g is the group velocity of the mode, obtained as:

$$n_g = n_{\text{eff}} - \lambda_{\text{res}} \frac{\partial n_{\text{eff}}}{\partial \lambda} \tag{3}$$

3. Performance metrics

There have been different approaches towards defining a set of standard performance metrics for refractive index sensors [2,20,21]. The objective metrics described below can be used to evaluate the suitability of a biosensor and whether improvements have been achieved.

3.1. Sensitivity

The sensitivity of waveguide sensors depends on the extent of overlap of the evanescent field with the sample to be analysed [22,21]. The refractive index sensitivity (S), expressed in units of nanometres per refractive index unit (nm/RIU), is defined as:

$$S = \frac{\Delta\lambda_{\text{res}}}{\Delta n_{\text{clad}}} \tag{4}$$

where Δn_{clad} is the refractive index change of the cladding solution and $\Delta\lambda_{\text{res}}$ is the resulting resonant wavelength shift.

The evanescent wave extends only to a short distance (between tens and hundreds of nanometres depending on the waveguide size and the involved wavelength) from the interface, and its power decreases exponentially with distance from the surface, as can be appreciated in Fig. 4. The bulk refractive index sensitivity is the maximum possible refractive index sensitivity value, since it is obtained by modifying the index of the waveguide surroundings in bulk. In a real setting, liquids virtually cover the whole evanescent field region, reaching a maximum sensitivity, which corresponds with the horizontal asymptote of the characteristic exponential curve of the evanescent field (see Fig. 4). Thus, the so-called bulk sensitivity is calculated according to Eq. (4).

Although the bulk sensitivity is relatively simple to measure and can be used to compare with other label-free methods, it is merely an estimate for the sensitivity in real biomolecular assays [24]. In these cases, surface sensitivity is obtained instead, which considers the resonant wavelength shift caused by a refractive index change only on the surface of the RR waveguide core. Due to the broad range of biochemical assays, there is not a single definition of surface sensitivity, as the thickness and the refractive index of the biolayer are dependent on the biomolecules used in the assay [23,15]. In this work, the definition adopted for the calculation of surface sensitivity

Biomedical Optics EXPRESS

is based on Eq. (4) as well, enabling a more direct comparison with the bulk sensitivity, where Δn_{clad} is the difference in refractive index between the biolayer with a constant thickness and the buffer solution, and $\Delta\lambda_{res}$ is the measured peak displacement caused by the biolayer deposition.

Finally, to compare resonators working at different wavelengths, the normalised sensitivity, S', which is the sensitivity of the resonator divided by its operating wavelength, is usually used:

$$S' = \frac{S}{\lambda_{res}} = \frac{1}{n_g}\frac{\partial n_{eff}}{\partial n_{clad}} \tag{5}$$

3.2. Quality factor

The degree of interaction of light with the sample in RRs is not limited by the length of the sensing waveguide, but rather by the number of oscillations the guided light can complete before decay. The quality factor, Q, a measure of photon lifetime in the RR, is inversely proportional to loss and represents the number of oscillations before the energy of the photon decays to 37% [16]. The quality factor is a dimensionless value which takes into account the coupling losses and the intrinsic losses (through radiation, scattering and absorption) [25] in terms of the material's index of refraction [2], and is obtained experimentally by:

$$Q = \frac{\lambda_{res}}{\Delta\lambda} \tag{6}$$

where $\Delta\lambda$ is the full width half maximum of the corresponding resonance (nm). Therefore, the quality factor is a measure of the sharpness of the resonance relative to its central wavelength. A higher Q improves the minimal detectable wavelength shift and reduces the sensor's spectral noise [22], enhancing the sensing performance. High Q photonic cavities (of the order of magnitude of 10^3 and above) can be achieved through precise fabrication, favouring a significant increase in the effective optical path length as well as a sharpening of the resonance to a narrow spectral dispersion. This allows smaller shifts caused by smaller binding-induced changes in n_{eff} to be discerned [26].

3.3. Limit of detection

The system's limit of detection (sLOD) is defined as the minimum refractive index change ($\Delta n_{clad,min}$) necessary to cause a detectable change in the output signal. Its value depends on system factors and is related with the readout instrumentation and the experimental set-up. Hence, it is complicated to objectively compare sensors characterised using different experimental systems and equipment. Instead, the intrinsic limit of detection (iLOD), which only depends on intrinsic resonator characteristics, can be calculated as [15]:

$$\text{iLOD} = \frac{\lambda_{res}}{QS} \tag{7}$$

which leaves the iLOD with units of RIU. An improved sensor performance is characterised by a lower iLOD, enabling a quantitative comparison of different resonant sensors.

4. Numerical analysis

Figure 1 (a) shows a scanning electron microscope (SEM) image of the device under study a RR of 1028 μm length coupled to a bus waveguide via a multimode interferometer (MMI) coupler (see a detailed image of this section in Fig. 1 (b)). The waveguides, which rest on a silicon dioxide lower cladding, have a rectangular cross-section with thickness $t = 300$ nm and width $w = 1100$ nm. The fabrication process is based on a direct writing electron beam process on a poly-methyl methacrylate (PMMA) positive resist layer with a thickness of 100 nm. After developing the resist, a metal mask was created by chromium evaporation prior to a lift-off

Biomedical Optics EXPRESS

process. This metal mask was used to perform the inductively coupled plasma-reactive ion etching (ICP-RIE) of the silicon nitride layer using fluoride gases. With the mentioned process, we got propagation losses ~2.5 dB/cm in the fabricated samples. Finally, after depositing a 1 μm SiO_2 layer by plasma enhanced chemical vapor deposition, a circular window aimed at sensing was opened on the RR by removing the SiO_2 with a second e-beam lithography and a new ICP-RIE etching step.

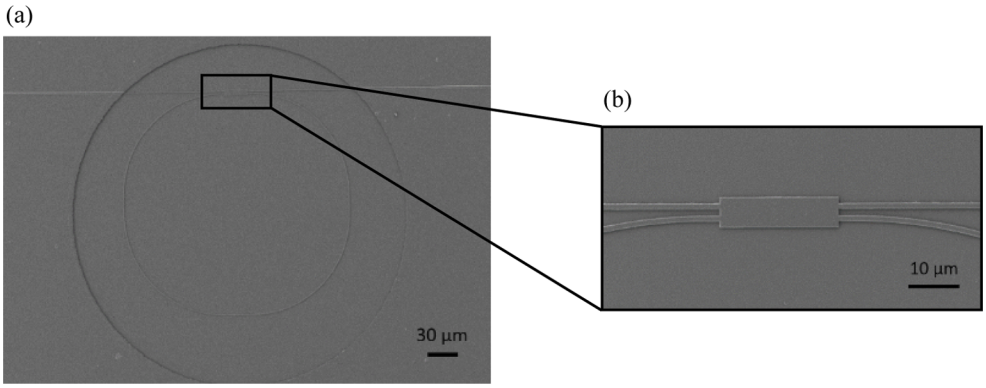

Fig. 1. SEM images of the device under study. (a) RR coupled to the bus waveguide. (b) Detail of the MMI.

Our objective is to compare the performance as a sensor of a silicon nitride RR operating around 1550 nm using the TE mode (as in most works reported so far) and at 1310 nm using the TM mode. This requires in a first step that the waveguides support guided modes in these two regimes, which is confirmed in the numerical simulations performed using RSoft (Fig. 2). According to the dimensions of the waveguides used, the TM mode is not guided at 1550 nm wavelengths, but the TE mode can be propagated at 1310 nm, so simulations and experiments have also been carried out under these conditions to reveal the origin of the sensitivity improvement. Additionally, the device should display a similar behaviour in these different conditions, which requires the MMI to operate approximately in a 50:50 fashion. We then calculated the response of the MMI for both TE and TM modes using the finite difference time domain (FDTD) method. The results are given in Fig. 2. The power (normalized with respect to a single waveguide) at the ring and bus waveguide outputs of the MMI operated in the 1310 nm regime at TM mode are 0.391 and 0.366, respectively (as shown in Fig. 2 (c)), which give 51.7% and 48.3% coupling ratios. Therefore, compared to working with TE mode at 1550 nm (Fig. 2 (a)), the coupling ratio is closer to the ideal value of 50%, and the ratio of the power obtained at the output with respect to the absence of MMI is higher. This means that the MMI already works optimally at the new working conditions (propagating TM mode at 1310 nm), so no further optimisation is required and, more importantly, we can use the RR for our comparison purposes.

A theoretical sensitivity analysis was carried out by simulating the effective refractive index of the fundamental TE and TM modes at 1550 nm and 1310 nm wavelengths, respectively, using the finite element method (FEM). A distinction was made between bulk and surface sensitivity, which present different simulation scenarios and parameter values.

4.1. Theoretical bulk sensitivity

Given that the mode's evanescent field overlap with the cladding determines the sensitivity of the sensor, from the mode profiles in Fig. 2 (a) and Fig. 2 (b) it is apparent that the TM mode electric field extends further into the uppercladding than the TE mode. This demonstrates the significant sensing advantage of the TM mode for molecular add-layers or large biomolecules [2].

Biomedical Optics EXPRESS

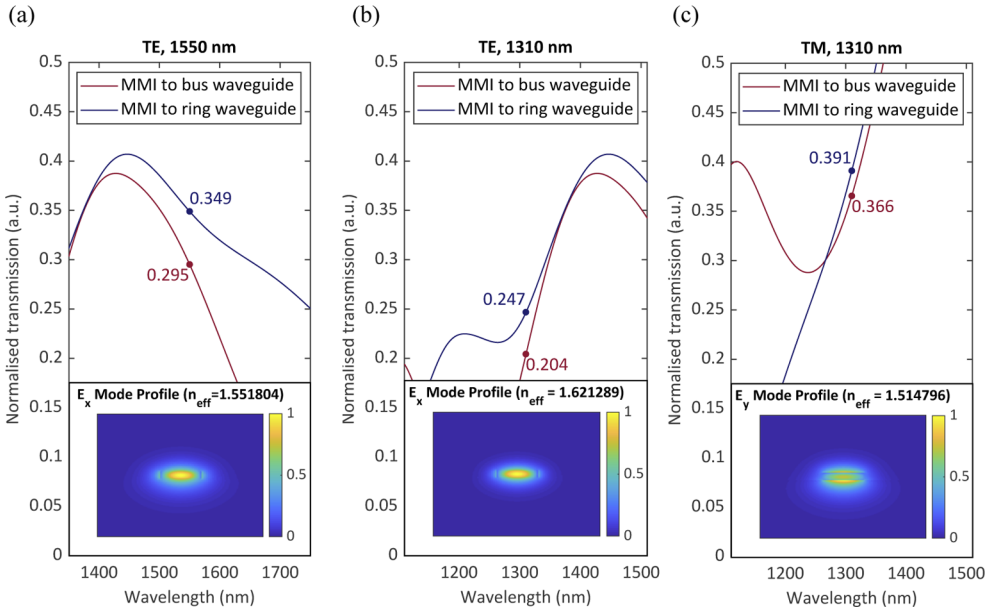

Fig. 2. FDTD simulation results showing the normalised power transmission across the MMI, along with the electric field profiles (insets) of the fundamental modes of the waveguide for (a) the TE mode around 1550 nm, (b) the TE mode around 1310 nm and (c) the TM mode around 1310 nm wavelengths. An uppercladding index of 1.32 (water) was employed in the simulations to account for the biological buffer solutions used in real experiments. In the insets, the horizontal (vertical) electric field is shown for the TE (TM) mode.

By combining Eq. (3) and Eq. (5), the sensitivity, S, obtained from simulations can be quantified according to the following expression:

$$S = \frac{1}{n_{\text{eff}} - \lambda_{\text{res}} \frac{\partial n_{\text{eff}}}{\partial \lambda}} \frac{\partial n_{\text{eff}}}{\partial n_{\text{clad}}} \lambda_{\text{res}} \tag{8}$$

The parameter n_{eff} is obtained directly from the FEM simulations while the derivative terms can be approximated by simulating the variation of n_{eff} against λ and n_{clad}, respectively, as shown in Fig. 3. Both structural and material dispersion have been considered in our calculations. It should be noted that the variations of n_{eff} with λ, shown in Fig. 3(a), are dependent on other variables, such as n_{clad}. However, since a short wavelength span is being considered, a linear fit is used to calculate the derivative terms around the working wavelengths (either 1310 nm or 1550 nm). We have also neglected water absorption which should lead to an imaginary effective index. Even though such imaginary index should not affect the sensitivity, it should change the Q factor thus altering the iLOD. Since the system would become more complex, mainly due to the interplay between the MMI coupling ratio and the waveguide losses in the Q factor, we prefer to neglect absorption losses here and leave a more detailed analysis for further work. Still, the simulations support our experimental results in a highly consistent way so the main claims of our wok are perfectly valid.

The simulation results shown in Fig. 2 and Fig. 3 were used to calculate the bulk sensitivity according to Eq. (8). The bulk sensitivities obtained were 192.08 nm/RIU for TM mode at 1310 nm, 163.05 nm/RIU for TE mode at 1550 nm, and 93.80 nm/RIU for TE mode at 1310 nm. Therefore, in theory, a sensitivity improvement of approximately 17.8% was expected when using the TM mode at 1310 nm compared to TE mode at 1550 nm.

Biomedical Optics EXPRESS

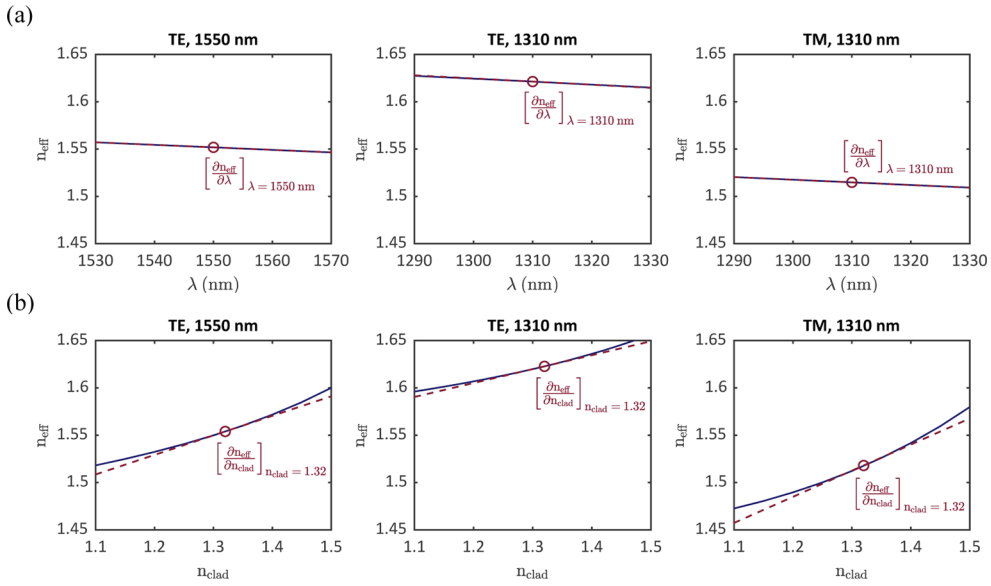

Fig. 3. Effective refractive index change with respect to (a) variations in the wavelength of light and (b) variations in the refractive index of the cladding, for TE mode at 1550 nm, TE mode at 1310 nm and TM mode at 1310 nm wavelengths. The blue solid lines represent the simulation results whereas the red dashed lines are the tangents at the points marked with circles, used to calculate the derivative terms shown.

Furthermore, the theoretical FSR was calculated to deduce, by comparison with experimental FSR, whether the polarisation being measured corresponded to the simulated one. In other words, to confirm that either the TE or the TM mode was being propagated in the waveguides. By combining Eq. (2) and Eq. (3) and given that the physical length of the RR is 1028 μm, the FSR calculated for TE mode at 1550 nm was 1.19 nm whilst the FSR calculated for TM mode at 1310 nm was 0.89 nm.

4.2. Theoretical surface sensitivity

Due to the high variety of biosensing assays, surface sensitivity is usually defined for a specific molecule or antigen-antibody reaction. In this work, the bovine serum albumin (BSA)-anti-bovine serum albumin (antiBSA) pair was used as a model to calculate the surface sensitivity of the sensor. BSA is an albumin with a molecular weight of 66.5 kDa, thereby being a globular protein soluble in water and moderately soluble in concentrated salt solutions [27]. AntiBSA is an immunoglobulin type IgGA [28] with a molecular weight of 160 kDa which acts as a specific antibody for BSA [27]. Phosphate-buffered saline (PBS) was used as a buffer for the reagents to be flowed over the sensor surface. Therefore, the background index for the simulations was set to 1.34, which corresponds to the refractive index of PBS [29].

It has been suggested that, once the BSA-antiBSA recognition reaches the saturation stage, the layer formed has a total thickness ranging from 14 nm to 16 nm [30]. Although the exact refractive index of the layer formed by the BSA-antiBSA pair has not been determined, the values usually range from 1.40 to 1.41 for a generic adsorbed layer of proteins [27,30]. Hence, for the simulations in this work, a 15-nm thick layer with a refractive index of 1.41 was considered, which has been proved to correspond well with experimental results when modelling a monolayer consisting of the BSA-antiBSA pair [31]. Although the geometry of the binding molecules could have been considered to achieve a more realistic model [32], the concentrations of reactants used

Biomedical Optics EXPRESS

in experiments ensure the saturation of the surface, so the simulation of a single biolayer is a suitable approximation in this case.

Moreover, since it is not clear whether the biomolecules are preferentially adsorbed on the upper or the side surfaces of the waveguide, both models were considered in the simulations, to determine which one gets closer to experimental results. For each scenario, the sensitivity was calculated as a function of the biofilm thickness. This involved performing a series of simulations for discrete biofilm thicknesses to then calculate the sensitivity in each case by applying Eq. (8). Once an adequate number of points (corresponding to different biolayer thicknesses) were obtained, the data was fitted with an exponential model, where the high correlation coefficients reflect the exponential nature of the evanescent field. This enables to contextualize the theoretical sensitivity values calculated for a 15 nm-thick biolayer (used to model the BSA-antiBSA layer), as well as illustrating the relationship between the surface and bulk sensitivities. The BSA-antiBSA assay results will be used to validate the model, which could be applied to further experiments using other proteins generating different biolayer thicknesses.

Figure 4 shows the evolution of the sensitivity with an increasing biolayer thickness for TM mode at 1310 nm and TE mode at 1550 nm, adding the layer only on top of the waveguide or throughout the whole surface area (including the sides as well as the top). The surface sensitivity approaches the bulk sensitivity (which corresponds to the asymptote of the exponential curve) for large biolayer thicknesses. As mentioned above, the evanescent field concentrates at the top surface and not as much at the sides for the TM mode profile, whilst the TE mode presents a more evenly distributed evanescent field around the waveguide. Therefore, it makes sense that a higher percentage increase in sensitivity (from TE mode at 1550 nm to TM mode at 1310 nm) is expected if only top surface coverage is considered. Also, it is understandable that the model considering only top surface coverage does not reach bulk sensitivity, since the evanescent field leaving through the sides of the waveguide is not occupied by the biolayer, hence losing that potential component of sensitivity.

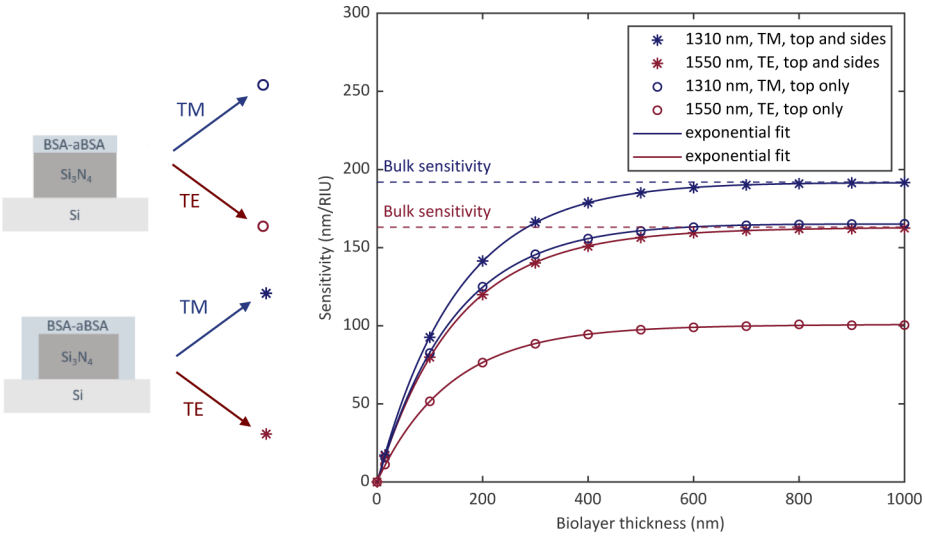

Fig. 4. Surface sensitivities as a function of the biolayer thickness for different scenarios, approaching the corresponding bulk sensitivities for thicker biolayers.

Biomedical Optics EXPRESS

5. Experimental results

5.1. Experimental set-up

The set-up used to measure at different polarisations on the same photonic integrated circuit (PIC) involves coupling light from the optical fibre to the waveguides at the edge of the chip. The output light is imaged by an objective lens and a camera, as well as being directed towards a power meter. A schematic of the set-up is shown in Fig. 5. The wavelength range of the laser used includes both the 1310 nm and 1550 nm regimes.

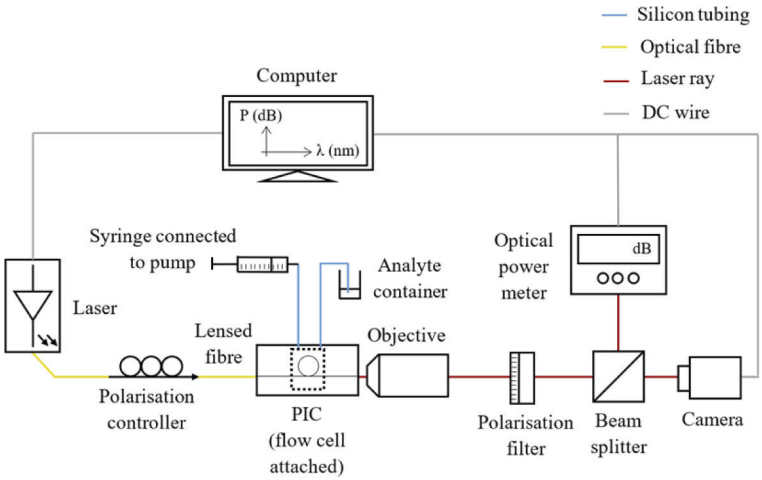

Fig. 5. Schematic of the experimental set-up used to test the RRs as sensors.

The polarisation filter is used, along with the polarisation controller, to cancel the opposite polarisation to the one desired. When the desired polarisation is fixed, a wavelength sweep is performed, and the transmission spectrum is recorded. The power meter measures the output power in dB units (for 0 dBm input power), which is represented on the computer along with the wavelength of the laser, using a software based on LabView.

To characterise the performance in aqueous media and obtain the bulk and surface sensitivities, the sensors were subjected to ethanol solutions at different concentrations as well as BSA and antiBSA via a microfluidic channel. A custom flow cell, composed of a double-sided adhesive with a central channel (7×1.5 mm) alongside a piece of methacrylate with two transversal holes (an inlet and an outlet) matching the distance between the ends of the channel, was used to create a fluidic channel on the chip. The required tubing to connect the microfluidic channel with the pump and the analyte container to handle the fluidics properly was inserted through the inlet and the outlet of the methacrylate piece. It was silicone elastomer tubing (with an inner and outer diameter of 0.51 mm and 0.94 mm, respectively) matching to the inner diameter of the inlet and the outlet. The whole fluidic system was assembled by attaching one side of the double-sided adhesive tape to the chip, leaving the RRs centred at the channel and, subsequently, the other side to the methacrylate piece with the tubing. A syringe pump was operated in withdrawal mode to pull solutions across the sensors at a controlled flow rate (between 10 and 20 µL/min). It should be noted that all experiments were carried out at room temperature (23°C), with minor fluctuations which are not sufficiently intense or rapid to require compensation.

5.2. Experimental bulk sensitivity

To assess the bulk sensitivity to refractive index changes in the cladding, the RRs were subjected to a set of ethanol solutions of varying concentrations. Before starting with the actual experiments,

Biomedical Optics EXPRESS

the sample was characterised in a water medium and one of the RRs was selected to perform all the sensing experiments. While data from a single RR is represented in this section for clarity and to ensure the validity of the measurements, each tested RR behaved in a similar fashion. Then, the polarisation controller and filter were used to guide TE- or TM-polarised light. Due to the dimensions of the waveguide, both TE and TM modes are supported at 1310 nm wavelengths, whereas only TE mode can be guided at 1550 nm wavelengths. Therefore, at 1310 nm, it is necessary to employ the filter to ensure that only TM-polarised or TE-polarised light propagates.

After the preliminary measurements in water, transmission spectra were recorded while flowing ethanol 5% and 10% solutions, for a wavelength span of 40 nm, centred at 1550 nm or 1310 nm, using a step of 0.05 nm. These measurements are shown in Fig. 6 (a), for TE mode at 1550 nm, and Fig. 6 (b), for TM mode at 1310 nm. The fact that the reference spectrum obtained with distilled water is displaced by a constant value when flowing the ethanol solutions demonstrates that the wavelength shift measured for a single resonant peak is representative of the whole spectrum around the central wavelength. Also, these measurements suggest that the selected concentrations are adequate for the experiment since the refractive index difference is detected. Based on these results, it was decided to use a wavelength span of 2 nm to make the experiment feasible in terms of time, and a step of 0.01 nm (the minimum possible) to reduce the ambiguity when determining the peak position.

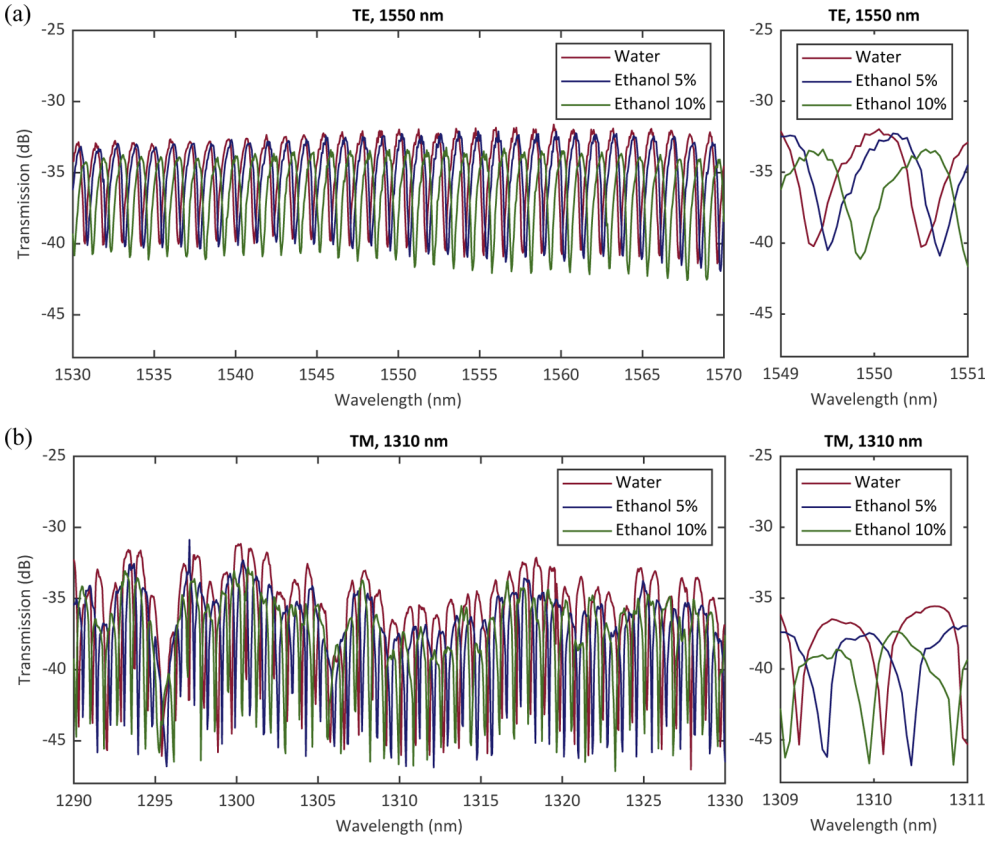

Fig. 6. Transmission spectra of a RR exposed to surrounding media of water, ethanol 5% and ethanol 10% for (a) the TE mode at 1550 nm wavelengths and (b) the TM mode at 1310 nm wavelengths. Note that the same figures are represented for a narrower wavelength span for clarity purposes.

Biomedical Optics EXPRESS

Finally, the sensing experiment was performed with ethanol solutions prepared in concentrations of 2%, 4%, 8%, 16% and 32% in volume. The sensors were exposed to the solutions at a flow rate of 20 µL/min. Three experiments were performed under the same conditions to obtain a mean output value and the associated dispersion. The raw data in the form of transmission spectra were processed to track the wavelength shift of a single resonant peak, as shown in Fig. 7. The refractive indices of the water and ethanol solutions employed were found at 1310 nm and 1550 nm wavelengths, to plot the resonance peak wavelength shifts against the refractive index change of each solution with respect to distilled water. The refractive indices of distilled water are 1.3223 and 1.3180, at 1310 nm and 1550 nm, respectively [33]; whereas the refractive indices of pure ethanol are 1.3520 and 1.3507, at 1310 nm and 1550 nm, respectively [34]. These values are summarised in Table 1, along with the corresponding densities.

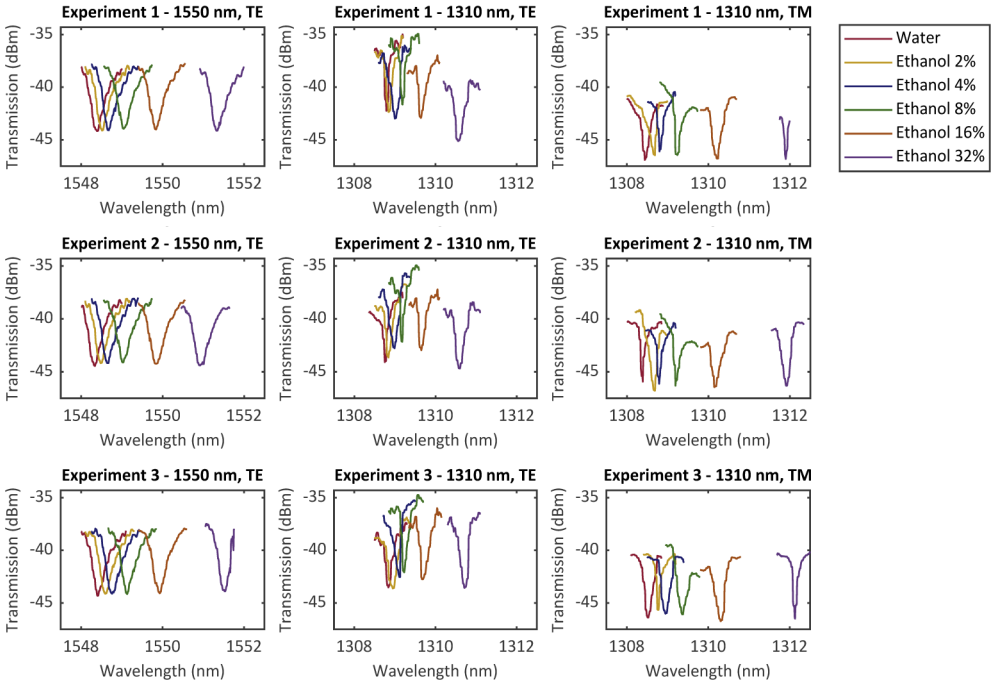

Fig. 7. Sensing experiments with distilled water and ethanol solutions, tracking the displacement of a resonant peak, for TE mode at 1550 nm, TE mode at 1310 nm and TM mode at 1310 nm.

Table 1. Densities and refractive indices at 1310 nm and 1550 nm for pure ethanol and distilled water.

	Ethanol	Water
Density (g/l)	789	997
RI at 1310 nm	1.3520	1.3223
RI at 1550 nm	1.3507	1.3180

To obtain the refractive indices of the ethanol solutions, the concentrations in % volume, $c_{\%\text{volume}}$, were first converted to concentrations in % mass, $c_{\%\text{mass}}$, according to:

$$c_{\%\text{mass}} = \frac{c_{\%\text{volume}}\rho_{\text{ethanol}}}{\frac{c_{\%\text{volume}}}{100}\rho_{\text{ethanol}} + \left(1 - \frac{c_{\%\text{volume}}}{100}\right)\rho_{\text{water}}} \tag{9}$$

Biomedical Optics EXPRESS

where ρ_{ethanol} and ρ_{water} are the densities of pure ethanol and distilled water, respectively, as given in Table 1. Then, the refractive index of the corresponding ethanol solution, n_{solution}, was estimated by [35]:

$$n_{\text{solution}} = 1.024\frac{c_{\%\text{mass}}}{100}n_{\text{ethanol}} + \left(1 - \frac{c_{\%\text{mass}}}{100}\right)n_{\text{water}} \tag{10}$$

where n_{ethanol} and n_{water} are the refractive indices of pure ethanol and distilled water, respectively, as given in Table 1. The calculations performed according to Eq. (9) and Eq. (10) are summarised in Table 2, where the difference between the refractive index of the corresponding ethanol solution and the refractive index of water is finally obtained.

Table 2. Calculation of the refractive index change of each ethanol solution with respect to distilled water at 1310 nm and 1550 nm wavelengths.

Wavelength (nm)	Ethanol % volume	Ethanol % mass	RI solution	RI solution – RI water
1310	2	1.5894	1.3233	0.0010
	4	3.1921	1.3243	0.0020
	8	6.4385	1.3263	0.0040
	16	13.0992	1.3304	0.0081
	32	27.1355	1.3392	0.0169
1550	2	1.5894	1.3190	0.0010
	4	3.1921	1.3201	0.0021
	8	6.4385	1.3222	0.0042
	16	13.0992	1.3265	0.0085
	32	27.1355	1.3357	0.0177

The resonant peak displacement values (represented in Fig. 7) were plotted against the refractive index change of each ethanol solution with respect to distilled water (the last column in Table 2), as shown in Fig. 8. The sensor sensitivity to refractive index was determined by the slope of the linear fit and is 164.8 nm/RIU for TE at 1550 nm and 210.2 nm/RIU for TM at 1310 nm, which implies a sensitivity increase of 27.6%, even higher than the simulation predictions. We attribute the difference between simulations and experiments to fabrication inaccuracies as well as uncertainties in the determination of the refractive index of the employed solution from the concentrations. Still, the fact that the bulk sensitivity for the TE mode at 1310 nm is the lowest suggests that it is the polarisation change from TE mode to TM mode that causes a sensitivity improvement.

Furthermore, the FSR, for both the TE mode at 1550 nm and the TM mode at 1310 nm, was also obtained by fitting the resonant peaks from the transmission spectra measured in a water medium with Lorentz functions. The FSR calculated for the TE mode at 1550 nm wavelengths is 1.18 nm, which is very close to the predicted value of 1.19 nm. In the case of the TM mode at 1310 nm, the experimental FSR was 0.86 nm, which compared with the theoretical value of 0.89 nm. This close agreement between theoretical and experimental FSR values confirms that TE- and TM-polarised light was guided so the experimental results are valid.

Moreover, the measured S and Q values were used to calculate the iLOD according to Eq. (7). The Q factors around 1310 nm and 1550 nm extracted from the spectra are 4965 and 2575, respectively. Therefore, under the TM mode regime at 1310 nm wavelengths, both the sensitivity and quality factor have increased with respect to the TE mode at 1550 nm, as was hypothesised. This implies reducing the iLOD from 3.65×10^{-3} RIU to 1.26×10^{-3} RIU.

Biomedical Optics EXPRESS

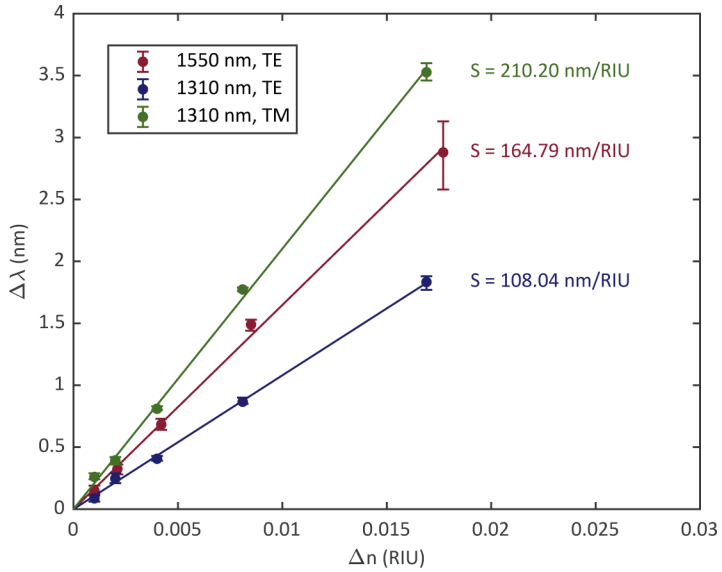

Fig. 8. Resonant wavelength shift plotted against the corresponding change in refractive index of each ethanol solution with respect to distilled water.

5.3. Experimental surface sensitivity

After performing the sensing experiments with ethanol solutions, a more practical experiment was carried out to measure the surface sensitivity of the sensor to biomolecules, thus demonstrating its ability to interrogate biomolecular interactions. The sensors can be coated with biological receptors by flowing the solutions containing the biomolecules over the RRs.

Preliminary measurements were made on PBS buffer to select a wavelength window, reaching a trade-off between reducing time and appropriately tracking the resonant peak. Eventually, a 2-nm window was selected, and a wavelength step of 0.01 nm was set to perform consecutive measurements. Since each measurement took approximately 1.7 minutes to complete, by flowing the reagents and buffers through the microfluidic delivery system at a rate of 10 µL/min, a satisfactory approximation to real-time monitoring was achieved. The reagents used for the experiment were 15 µM BSA and 50 nM antiBSA, as well as PBS 1x buffer. BSA and antiBSA stock solutions were prepared the same day of the experiments and two separate samples were extracted from each, to guarantee that the concentrations were exactly the same for both experiments (for TE mode at 1550 nm and TM mode at 1310 nm). A large concentration of BSA was employed to limit non-specific interactions of antiBSA with the surface of the resonator.

The biosensing experiment required a series of steps to finally obtain the sensorgram represented in Fig. 9. The biomolecules are simply physically adsorbed to the surface, without involving any kind of covalent immobilization, so no previous surface treatments are employed. The first stage involved equilibrating the sensor using PBS buffer for 10 minutes to establish a signal baseline in the sensorgram. Next, the BSA was introduced for 30 minutes, and a shift in the resonance wavelength was observed, indicating a successful detection. This was followed by a 20-minute PBS rinse, where the first 10 minutes enabled the removal of any unbound protein and the last 10 minutes allowed to establish a signal baseline in the sensorgram before flowing the next reagent. Then, the antiBSA was passed over the BSA-functionalised sensor for 30 minutes, and the selective binding to the BSA generated another irreversible shift in the resonance wavelength. Air bubbles were unintendedly introduced mid-way through the antiBSA cycle. Despite not altering subsequent biological interactions, these events modify the transmission spectrum, so

Biomedical Optics EXPRESS

the corresponding measurements have been omitted from the sensorgram. Finally, PBS was introduced for 10 minutes to remove any unbound antiBSA molecules from the fluidic channel.

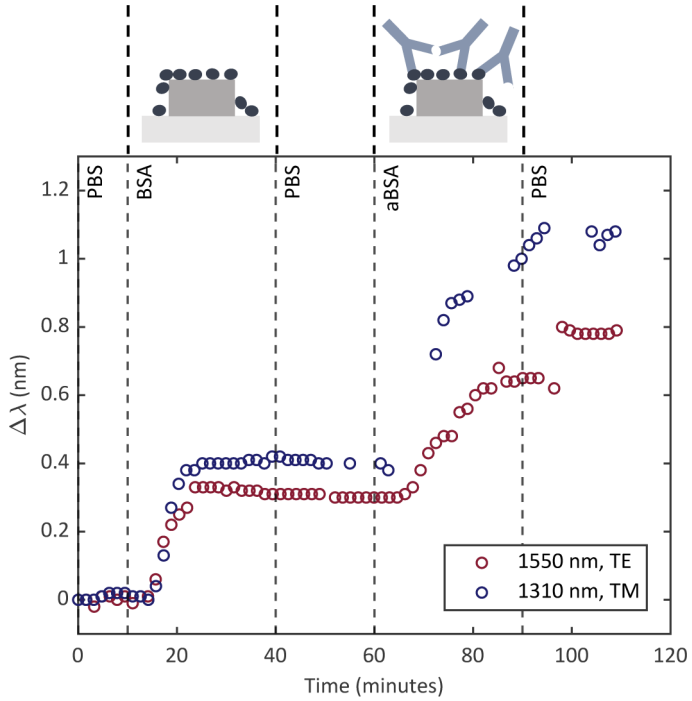

Fig. 9. Sensorgram obtained from BSA-antiBSA experiments for the TE mode at 1550 nm and the TM mode at 1310 nm. The dashed vertical lines represent the region boundaries involving a change in the flowed solution, and it takes around 8 minutes for the new solution to reach the sensor (according to the flow rate and the length of the silicon tubing used).

The surface sensitivity can be calculated from the obtained sensorgram. A permanent resonant wavelength shift of approximately 0.79 nm remains after the final PBS buffer rinse for the TE mode at 1550 nm, whereas a final displacement of 1.07 nm is recorded for TM mode at 1310 nm. This involves a surface sensitivity increase of 35.4% when propagating TM mode at 1310 nm, compared to the TE mode at 1550 nm, the original operating conditions. Similar sensitivity increase values are obtained considering the wavelength shift induced by BSA only (33.3%) and antiBSA only (36.7%). The corresponding sensitivity values can be calculated according to Eq. (4), by dividing the resonance shift (RR with the BSA-antiBSA layer compared to RR in initial buffer) by the refractive index difference between the biolayer (1.41) and the ambient PBS medium (1.34). The resulting surface sensitivity values, which correspond with a biolayer thickness of 15 nm, are 11.3 nm/RIU and 15.3 nm/RIU, for the TE mode at 1550 nm and the TM mode at 1310 nm, respectively. These values are represented in Fig. 10, along with the two models (biolayer deposited on the top and sides of the waveguide or on the top only) simulated and previously represented in Fig. 4.

The comparison between simulations and experimental sensitivities with a biolayer thickness of 15 nm shown in Fig. 10 suggests that the model where only the top surface is covered by the biolayer is closer and even coincident with the measured values. If this model were considered, the increase in sensitivity from TE mode at 1550 nm to TM mode at 1310 nm would be larger compared to the model where the biolayer is also deposited on the sides of the waveguide. However, further experiments should be conducted to conclude whether one or the other model

Biomedical Optics EXPRESS

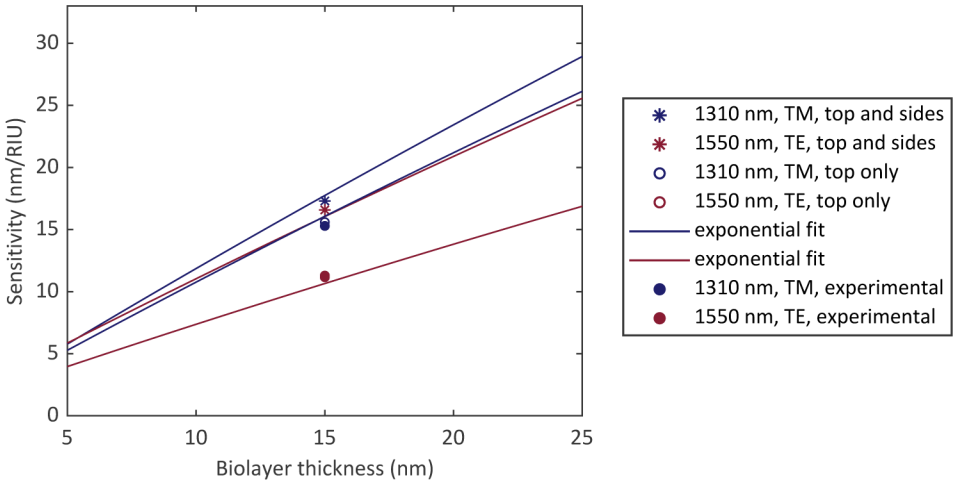

Fig. 10. Sensitivity as a function of the biolayer thickness for different simulated scenarios, along with the values obtained experimentally. The theoretical values are fitted with an exponential model, following from Fig. 4.

is more likely to occur. As it can be deducted from Fig. 4, a biolayer with a larger thickness would enable to discriminate better between one model or the other, since the corresponding sensitivities are more distant, hence less susceptible to the influence of errors. Therefore, future experiments could involve adding an intermediate layer of protein A [27], or even an interlayer composed of an electrostatic self-assembled film [36].

6. Conclusions

We have demonstrated an improved performance for a Si_3N_4 RR sensor by using the TM mode at 1310 nm wavelengths instead of the TE mode at 1550 nm used in most experiments reported so far. A sensitivity improvement results from a larger component of the evanescent field traveling above the waveguide for TM mode compared to TE mode. Also, using 1310 nm wavelengths instead of 1550 nm reduces losses due to the absorption of water in aqueous analytes, thus increasing the RR Q factor, as well as being a more cost-effective alternative.

The experimental bulk sensitivity of the sensor is 164.8 nm/RIU for TE mode at 1550 nm and 210.2 nm/RIU for TM mode at 1310 nm, which implies an improvement of 28%. The surface sensitivity for the BSA-antiBSA model (which corresponds with a biolayer thickness of 15 nm) is 11.3 nm/RIU for TE mode at 1550 nm and 15.3 nm/RIU for TM mode at 1310 nm, which implies an increase of 35%. The quality factors extracted from the transmission spectra of the resonators in distilled water are 2575 for TE at 1550 nm and 4965 for TM at 1310 nm, implying an increase of 93%. Hence, under the TM mode regime at 1310 nm, both the sensitivity and quality factor increase with respect to the TE mode at 1550 nm. This means a reduction of 65% in the iLOD (from 3.65×10^{-3} RIU for TE mode at 1550 nm to 1.26×10^{-3} RIU for TM mode at 1310 nm), thus improving the overall performance of the sensor suited for lab-on-chip applications. This finding suggest that biosensors implemented in silicon-photonics could improve their overall performance by merely changing the operational wavelength and the employed mode.

Funding. Generalitat Valenciana (IDIFEDER/ 2018/033, IDIFEDER/2021/061, PROMETEO/2019/123); Ministerio de Ciencia, Innovación y Universidades (ICTS-2017-28-UPV-9); Horizon 2020 Framework Programme (958855).

Disclosures. The authors declare no conflicts of interest.

Biomedical Optics EXPRESS

Data availability. Data underlying the results presented in this paper are not publicly available at this time but may be obtained from the authors upon reasonable request.

References

1. A. L. Washburn and R. C. Bailey, "Photonics-on-a-chip: Recent advances in integrated waveguides as enabling detection elements for real-world, lab-on-a-chip biosensing applications," Analyst **136**(2), 227–236 (2011).
2. L. Chrostowski, S. Grist, J. Flueckiger, W. Shi, X. Wang, E. Ouellet, H. Yun, M. Webb, B. Nie, Z. Liang, K. C. Cheung, S. A. Schmidt, D. M. Ratner, and N. A. F. Jaeger, "Silicon photonic resonator sensors and devices," Laser Reson. Microresonators Beam Control XIV **8236**(February), 823620 (2012).
3. M. C. Estevez, M. Alvarez, and L. M. Lechuga, "Integrated optical devices for lab-on-a-chip biosensing applications," Laser Photonics Rev. **6**(4), 463–487 (2012).
4. A. Di Falco, L. O'Faolain, and T. F. Krauss, "Chemical sensing in slotted photonic crystal heterostructure cavities," Appl. Phys. Lett. **94**(6), 063503–95 (2009).
5. V. Toccafondo, J. García-Rupérez, M. J. Bañuls, A. Griol, J. G. Castelló, S. Peransi-Llopis, and A. Maquieira, "Single-strand DNA detection using a planar photonic-crystal-waveguide-based sensor," Opt. Lett. **35**(21), 3673 (2010).
6. G. Antonacci, J. Goyvaerts, H. Zhao, B. Baumgartner, B. Lendl, and R. Baets, "Ultra-sensitive refractive index gas sensor with functionalized silicon nitride photonic circuits," APL Photonics **5**(8), 081301 (2020).
7. S. M. Grist, S. A. Schmidt, J. Flueckiger, V. Donzella, W. Shi, S. Talebi Fard, J. T. Kirk, D. M. Ratner, K. C. Cheung, and L. Chrostowski, "Silicon photonic micro-disk resonators for label-free biosensing," Opt. Express **21**(7), 7994 (2013).
8. C. A. Barrios, M. J. Bañuls, V. González-Pedro, K. B. Gylfason, B. Sánchez, A. Griol, A. Maquieira, H. Sohlström, M. Holgado, and R. Casquel, "Label-free optical biosensing with slot-waveguides," Opt. Lett. **33**(7), 708 (2008).
9. F. P. Payne and J. P. R. Lacey, "A theoretical analysis of scattering loss from planar optical waveguides," Opt. Quantum Electron. **26**(10), 977–986 (1994).
10. G. Dabos, A. Manolis, A. L. Giesecke, C. Porschatis, B. Chmielak, T. Wahlbrink, N. Pleros, and D. Tsiokos, "TM grating coupler on low-loss LPCVD based Si3N4 waveguide platform," Opt. Commun. **405**, 35–38 (2017).
11. N. Daldosso, M. Melchiorri, F. Riboli, M. Girardini, G. Pucker, M. Crivellari, P. Bellutti, A. Lui, and L. Pavesi, "Comparison among various Si3N4 waveguide geometries grown within a CMOS fabrication pilot line," J. Lightwave Technol. **22**(7), 1734–1740 (2004).
12. S. Zheng, H. Chen, and A. W. Poon, "Microring-resonator cross-connect filters in silicon nitride: Rib waveguide dimensions dependence," IEEE J. Sel. Top. Quantum Electron. **12**(6), 1380–1387 (2006).
13. T. Taniguchi, A. Hirowatari, T. Ikeda, M. Fukuyama, Y. Amemiya, A. Kuroda, and S. Yokoyama, "Detection of antibody-antigen reaction by silicon nitride slot-ring biosensors using protein G," Opt. Commun. **365**, 16–23 (2016).
14. J. Zhu, S. K. Ozdemir, Y. F. Xiao, L. Li, L. He, D. R. Chen, and L. Yang, "On-chip single nanoparticle detection and sizing by mode splitting in an ultrahigh-Q microresonator," Nat. Photonics **4**(1), 46–49 (2010).
15. S. TalebiFard, S. Schmidt, W. Shi, W. Wu, N. A. F. Jaeger, E. Kwok, D. M. Ratner, and L. Chrostowski, "Optimized sensitivity of Silicon-on-Insulator (SOI) strip waveguide resonator sensor," Biomed. Opt. Express **8**(2), 500 (2017).
16. S. Schmidt, J. Flueckiger, W. Wu, S. M. Grist, S. Talebi Fard, V. Donzella, P. Khumwan, E. R. Thompson, Q. Wang, P. Kulik, X. Wang, A. Sherwali, J. Kirk, K. C. Cheung, L. Chrostowski, and D. Ratner, "Improving the performance of silicon photonic rings, disks, and Bragg gratings for use in label-free biosensing," Biosensing Nanomedicine VII **9166**(October), 91660M (2014).
17. I. Teraoka and S. Arnold, "Theory of resonance shifts in TE and TM whispering gallery modes by nonradial perturbations for sensing applications," J. Opt. Soc. Am. B **23**(7), 1381–1389 (2006).
18. J. A. Curcio and C. C. Petty, "The near infrared absorption spectrum of liquid water," J. Opt. Soc. Am. **39**(1), 83–88 (1932).
19. L. Kou, D. Labrie, and P. Chylek, "Refractive indices of water and ice in the 065- to 25-μm spectral range," Appl. Opt. **32**(19), 3531 (1993).
20. W. Bogaerts, P. de Heyn, T. van Vaerenbergh, K. de Vos, S. Kumar Selvaraja, T. Claes, P. Dumon, P. Bienstman, D. van Thourhout, and R. Baets, "Silicon microring resonators," Laser Photonics Rev. **6**(1), 47–73 (2012).
21. J. Hu, X. Sun, A. Agarwal, and L. C. Kimerling, "Design guidelines for optical resonator biochemical sensors," *Opt. InfoBase Conf. Pap.* 2009.10.1364/josab.26.001032
22. I. M. White and X. Fan, "On the performance quantification of resonant refractive index sensors," Opt. Express **16**(2), 1020–1028 (2008).
23. K. De Vos, I. Bartolozzi, E. Schacht, P. Bienstman, and R. Baets, "Silicon-on-Insulator microring resonator for sensitive and label-free biosensing," Opt. Express **15**(12), 7610 (2007).
24. Y. Nazirizadeh, F. von Oertzen, K. Plewa, N. Barié, P.-J. Jakobs, M. Guttmann, H. Leiste, and M. Gerken, "Sensitivity optimization of injection-molded photonic crystal slabs for biosensing applications," Opt. Mater. Express **3**(5), 556 (2013).
25. H. El Dirani, "Development of high quality silicon nitride chips for integrated nonlinear photonics," 2020.
26. A. L. Washburn, L. C. Gunn, and R. C. Bailey, "Label-free quantitation of a cancer biomarker in complex media using silicon photonic microring resonators," Anal. Chem. **81**(22), 9499–9506 (2009).

Biomedical Optics EXPRESS

27. R. Caroselli, J. G. Castelló, J. Escorihuela, M. J. Bañuls, Á. Maquieira, and J. García-Rupérez, "Experimental study of the oriented immobilization of antibodies on photonic sensing structures by using protein a as an intermediate layer," Sensors **18**(4), 1012 (2018).
28. G. H. Cross, N. J. Freeman, and M. J. Swann, "Dual Polarization Interferometry: A Real-Time Optical Technique for Measuring (Bio)molecular Orientation, Structure and Function at the Solid/Liquid Interface," in *Handbook of Biosensors and Biochips*, John Wiley & Sons, Ltd, 2008.
29. L. Diéauez, N. Darwish, M. Mir, E. Martínez, M. Moreno, and J. Samitier, "Effect of the refractive index of buffer solutions in evanescent optical biosensors," Sens. Lett. **7**(5), 851–855 (2009).
30. R. Casquel del Campo, "Biosensors based on vertically interrogated optofluidic sensing cells," 2012. [Online]. Available: http://oa.upm.es/14645/
31. J. Vörös, "The density and refractive index of adsorbing protein layers," Biophys. J. **87**(1), 553–561 (2004).
32. M. R. Foreman and F. Vollmer, "Theory of resonance shifts of whispering gallery modes by arbitrary plasmonic nanoparticles," New J. Phys. **15**(8), 083006 (2013).
33. G. M. Hale and M. R. Querry, "Optical constants of water in the 200-nm to 200-μm wavelength region," Appl. Opt. **12**(3), 555 (1973).
34. E. Sani and A. Dell'Oro, "Spectral optical constants of ethanol and isopropanol from ultraviolet to far infrared," Optical Materials **60**, 137–141 (2016).
35. J. García-Rupérez, V. Toccafondo, M. J. Bañuls, J. G. Castelló, A. Griol, S. Peransi-Llopis, and Á. Maquieira, "Label-free antibody detection using band edge fringes in SOI planar photonic crystal waveguides in the slow-light regime," Opt. Express **18**(23), 24276 (2010).
36. S. Maguis, G. Laffont, B. Carbonnier, K. Kham, T. Mekhalif, and P. Ferdinand, "Biofunctionalized tilted fiber Bragg gratings for label-free biosensing," Opt. Soc. Am. **16**(23), 113–114 (2008).